



# Biogenic Sulfur Gases as Biosignatures on Temperate Sub-Neptune Waterworlds

Shang-Min Tsai<sup>1</sup>, Hamish Innes<sup>2,3</sup>, Nicholas F. Wogan<sup>4,5</sup>, and Edward W. Schwieterman<sup>1,5,6</sup><sup>1</sup>Department of Earth and Planetary Sciences, University of California, Riverside, CA, USA<sup>2</sup>Freie Universität Berlin, Institute of Geological Sciences, Malteserstrasse 74-100, 12249 Berlin, Germany<sup>3</sup>Atmospheric, Oceanic and Planetary Physics, Department of Physics, University of Oxford, UK<sup>4</sup>Space Science Division, NASA Ames Research Center, Moffett Field, CA 94035, USA<sup>5</sup>Virtual Planetary Laboratory, University of Washington, Seattle, WA 98195, USA<sup>6</sup>Blue Marble Space Institute of Science, Seattle, WA, USA

Received 2024 February 16; revised 2024 March 21; accepted 2024 March 24; published 2024 May 2

## Abstract

Theoretical predictions and observational data indicate a class of sub-Neptune exoplanets may have water-rich interiors covered by hydrogen-dominated atmospheres. Provided suitable climate conditions, such planets could host surface liquid oceans. Motivated by recent JWST observations of K2-18 b, we self-consistently model the photochemistry and potential detectability of biogenic sulfur gases in the atmospheres of temperate sub-Neptune waterworlds for the first time. On Earth today, organic sulfur compounds produced by marine biota are rapidly destroyed by photochemical processes before they can accumulate to significant levels. Domagal-Goldman et al. suggest that detectable biogenic sulfur signatures could emerge in Archean-like atmospheres with higher biological production or low UV flux. In this study, we explore biogenic sulfur across a wide range of biological fluxes and stellar UV environments. Critically, the main photochemical sinks are absent on the nightside of tidally locked planets. To address this, we further perform experiments with a 3D general circulation model and a 2D photochemical model (VULCAN 2D) to simulate the global distribution of biogenic gases to investigate their terminator concentrations as seen via transmission spectroscopy. Our models indicate that biogenic sulfur gases can rise to potentially detectable levels on hydrogen-rich water worlds, but only for enhanced global biosulfur flux ( $\gtrsim 20$  times modern Earth's flux). We find that it is challenging to identify DMS at  $3.4 \mu\text{m}$  where it strongly overlaps with  $\text{CH}_4$ , whereas it is more plausible to detect DMS and companion byproducts, ethylene ( $\text{C}_2\text{H}_4$ ) and ethane ( $\text{C}_2\text{H}_6$ ), in the mid-infrared between 9 and  $13 \mu\text{m}$ .

*Unified Astronomy Thesaurus concepts:* [Exoplanet atmospheres \(487\)](#); [Exoplanet atmospheric composition \(2021\)](#); [Biosignatures \(2018\)](#)

## 1. Introduction

The Kepler mission revealed a large fraction of discovered planets with radii between Earth and Neptune (Howard et al. 2012; Thompson et al. 2018; Bean et al. 2021). Observed masses and radii indicate a population of sub-Neptunes likely containing water-rich interiors, while evolution models also point to the existence of these waterworlds on the population scale (Zeng et al. 2019; Venturini et al. 2020; Luque & Pallé 2022; Rogers et al. 2023). In particular, several such planets orbiting M dwarf stars receive comparable insolation<sup>7</sup> to Earth, placing them in their planetary systems' habitable zones (e.g., Table 1 in Madhusudhan et al. 2021). These temperate sub-Neptunes have sparked great interest in atmospheric characterization and the assessment of habitability. Given suitable climate conditions (Innes et al. 2023; Pierrehumbert 2023), these water-rich worlds could host surface water oceans below hydrogen-rich atmospheres—recently referred to as “Hycean” (Hydrogen ocean) worlds (Madhusudhan et al. 2021; Nixon & Madhusudhan 2021). Promisingly, their hydrogen-rich envelopes are more favorable for atmospheric characterization in transmission observations due to large scale heights, compared to the higher molecular weight  $\text{N}_2$ - or  $\text{CO}_2$ -dominated atmospheres.

Since the water detection in the atmosphere of the temperate sub-Neptune K2-18 b (Benneke et al. 2019; Tsiaras et al. 2019), follow-up analyses and modeling efforts have sought to unveil the nature of K2-18 b and similar temperate sub-Neptunes. Madhusudhan et al. (2020) explored the bulk composition under different interior structures. Tsai et al. (2021b) and Yu et al. (2021) proposed using atmospheric compositional evolution to infer the presence of a shallow surface, whereas Hu et al. (2021) investigated the carbon inventories in a Hycean planet scenario. Recent JWST transit observations revealed a strong detection of carbon dioxide ( $\text{CO}_2$ ) and methane ( $\text{CH}_4$ ) on K2-18 b (Madhusudhan et al. 2023). Based on this basis and upper limits of carbon monoxide ( $\text{CO}$ ) and ammonia ( $\text{NH}_3$ ), Madhusudhan et al. (2023) argued that the atmospheric characteristics of K2-18 b are more consistent with a Hycean world scenario. However, several inconsistencies warrant consideration: (1) It is challenging to accumulate a percentage level of  $\text{CH}_4$  without biological input or thermochemical recycling from the interior (Tsai et al. 2021b; Yu et al. 2021). (2) On Hycean planets,  $\text{CO}$  can still be efficiently produced to around 0.1%–1% level through photolysis of  $\text{CO}_2$ , while the quenched  $\text{CO}$  abundance is controlled by the interior temperature on Neptune-like planet with a thick ( $\gtrsim 100$  bar)  $\text{H}_2$  atmosphere (Wogan et al. 2024). (3) The cross-correlation method may be required to identify  $\text{CO}$  in JWST NIRSpec data (Esparza-Borges et al. 2023), while current analysis based on a single transit observation might not be sufficient to conclusively rule out  $\text{NH}_3$  before the upcoming MIRI and revisit observations (JWST Cycle 1, GO-2722, and GO-2372).

<sup>7</sup> Insolation from their host stars.

Intriguingly, Madhusudhan et al. (2023) also reported a tentative detection of dimethylsulfide (DMS), which is predominately produced by marine microbes on Earth and regarded as a biosignature gas, especially for anoxic biospheres (see Domagal-Goldman et al. 2011 and Schwieterman et al. 2018 for a review). On modern Earth, DMS is the main biological source of sulfur, about  $1.8\text{--}3.5 \times 10^9$  molecules  $\text{cm}^{-2}\text{s}^{-1}$  (Seinfeld & Pandis 2016; Cala et al. 2023). DMS and methanethiol ( $\text{CH}_3\text{SH}$ ) are released from the degradation of dimethylsulfoniopropionate (DMSP), an organosulfur compound produced by marine phytoplankton. Microbial methylation and detoxification processes can also actively produce DMS from hydrogen sulfide ( $\text{H}_2\text{S}$ ; Li et al. 2023), allowing hypothetical organisms to make use of the  $\text{H}_2\text{S}$  reservoir in a  $\text{H}_2$ -rich environment on Hycean worlds. In addition, decayed organic substances in the surface ocean can produce carbon disulfide ( $\text{CS}_2$ ) and carbonyl sulfide (OCS) through photochemical processes. These biosulfur gases are not directly associated with energy generation but are products or byproducts of physiological responses, referred to as Type III biosignatures in Seager et al. (2013). On present-day Earth, these organic sulfur gases are readily destroyed through photolysis or oxidation by OH radicals (Kettle et al. 2001; Domagal-Goldman et al. 2011) and thus cannot accumulate to significant concentrations exceeding the ppm level required for remote detection.

While great uncertainties persist regarding how biology could operate in an  $\text{H}_2$ -rich atmosphere, useful analogies can be drawn from anoxic environments on Earth. As early microbial life emerged, the Archean atmosphere was more reducing than the present-day atmosphere, with abundant  $\text{CO}_2$  and  $\text{CH}_4$  (e.g., Catling & Zahnle 2020). As indicated by genomic analysis, organic sulfur cycling could date back to the Proterozoic (Mateos et al. 2023), while sulfur-based metabolic pathways likely emerged in Earth's earliest biosphere in the Archean and may have been common for biological evolution (House et al. 2003; Pilcher 2003). On Archean Earth-like worlds, most biogenic sulfur gases are rapidly destroyed in the atmosphere similar to that of the present day, except with the major sink being the reaction with atomic O produced by photolysis (Domagal-Goldman et al. 2011). Curiously, the potential sulfur-based biosignatures and chemical pathways within a  $\text{H}_2$ -dominated atmosphere have not yet been fully explored with self-consistent photochemistry. Moreover, many close-in sub-Neptunes around M stars might be tidally locked. On the permanent nightside, such photochemical sinks of these organic sulfur gases do not exist. It is therefore essential to quantify whether the biogenic gases can build up on the terminators where transit observations probe.

In this Letter, we explore the global distribution and detectability of methane- and sulfur-based biosignature gases on Hycean planets through photochemical and climate modeling. While there is currently no robust evidence that K2-18 b is a Hycean planet, we adopt its properties as a paradigmatic example for Hycean exoplanets overall.

## 2. Methods

Here, we model the atmospheric composition of a Hycean planet under a range of biological surface emissions. Using the planetary parameters of K2-18 b as a fiducial example, we vary the surface flux of biosulfur gases and stellar UV flux to

quantify the impacts on the global composition of Hycean planet atmospheres.

### 2.1. 1D Climate and Photochemical Models

We iterate the radiative transfer (HELIOS; Malik et al. 2019a, 2019b) and photochemical (VULCAN; Tsai et al. 2017, 2021) models to obtain a self-consistent 1D temperature profile of Hycean K2-18 b. The radiative transfer model HELIOS has been modified to include the moist adiabatic lapse rate in the convective adjustment steps to simulate atmospheres with condensing components.<sup>8</sup> For our nominal Hycean planet, we assume a 1 bar  $\text{H}_2$ -dominated atmosphere with elements given by  $100\times$  solar metallicity, following Tsai et al. (2021b) and Yu et al. (2021). We fix the surface composition of  $\text{CO}_2$ ,  $\text{N}_2$ , and  $\text{H}_2\text{O}$  in the lower-boundary conditions.  $\text{CO}_2$  is set to 1% at the surface, based on the retrieved  $\text{CO}_2$  abundance in Madhusudhan et al. (2023) and in accordance with the carbon-inventory estimates in Kite & Ford (2018) and Hu et al. (2021). Surface  $\text{N}_2$  is fixed to 0.006, corresponding to all nitrogen (from the  $100\times$  solar metallicity) partitioning into  $\text{N}_2$ . The water vapor is assumed to be saturated above the ocean with a relative humidity of 50%. The spectrum of an analogous M2.5 star GJ 436 is adopted for both HELIOS and VULCAN.

To achieve a marginally habitable surface temperature, we employ an ad hoc surface albedo of 0.3, as previous studies have indicated that highly reflective clouds are necessary to prevent a runaway greenhouse state on K2-18 b (Piette & Madhusudhan 2020; Innes et al. 2023). Similarly, we do not account for the possibility of convection inhibition, which would otherwise raise the surface temperature beyond the supercritical point of water (Innes et al. 2023; Pierrehumbert 2023). This allowed us to model a habitable atmospheric state supportive of liquid surface water. The temperature and composition profiles are iterated between HELIOS and VULCAN until the temperature change is about 1%. The planetary parameters for our K2-18 b Hycean model are listed in Table A1.

The self-consistent temperature and composition structures of our “lifeless” K2-18 b Hycean planet (excluding biological surface fluxes) are illustrated in Figure B1. We then fed the temperature profile into VULCAN to model the compositional evolution in response to various biological surface fluxes. We updated the S-N-C-H-O photochemical network by revising the reactions involving  $\text{H}_2\text{CO}$  (see Appendix B and Wogan et al. 2024) and introduced reactions related to DMS and dimethyl disulfide (DMDS).<sup>9</sup> We consider  $\text{CH}_4$  released from methanogenesis and a range of organic sulfur gases biologically emitted from the surface, including  $\text{CH}_3\text{SH}$ ,  $\text{CS}_2$ , DMS, DMDS, and OCS, collectively termed “ $\text{S}_{\text{org}}$ ” after Domagal-Goldman et al. (2011). During this stage, the temperature profile from lifeless Hycean is held fixed and we neglect the thermal feedback from the compositional variations due to biological input (mainly  $\text{CH}_4$  and  $\text{S}_{\text{org}}$ ).

The rates of gases deposited to the ocean depend on the aerodynamics at the atmosphere–ocean interface and the solubility of the gas (Hu et al. 2012; Seinfeld & Pandis 2016). Due to the uncertainty of parameterizing the dry deposition velocities of several organic sulfur compounds, we assume zero

<sup>8</sup> <https://github.com/exoclimate/HELIOS/tree/development>

<sup>9</sup> [https://github.com/exoclimate/VULCAN/blob/master/thermo/SNCHO\\_DMS\\_photo\\_network\\_Tsai2024.txt](https://github.com/exoclimate/VULCAN/blob/master/thermo/SNCHO_DMS_photo_network_Tsai2024.txt)

dry deposition for  $\text{CH}_3\text{SH}$ , DMS, DMDS, and  $\text{CS}_2$ , corresponding to the upper limit of biosignature accumulation where biogenic sulfur compounds saturate the oceanic mixed layer. The lower-boundary conditions with modern Earth global average  $S_{\text{org}}$  flux are described in Appendix A and Table C1.

## 2.2. 3D GCM 2D Photochemical Model

In the absence of photochemical destruction, biological sulfur compounds can in principle build up on the nightside of a tidally locked Hycean planet. Global circulation plays a central role in transporting species between the dayside and nightside, where distinct chemical sources and sinks are at play (Chen et al. 2018; Tsai et al. 2021b, 2023c). To account for the day–night transport, we run VULCAN 2D (Tsai et al. 2021b, 2024) to model the equatorial region, using temperature and wind structures from the 3D general circulation model (GCM) Exo-FMS (Lee et al. 2021; Innes & Pierrehumbert 2022) as input.

Exo-FMS has previously been used to model the climate of a warmer K2-18 b (surface temperature  $>500$  K) without a liquid ocean and water condensation (Innes & Pierrehumbert 2022). In this study, we fit the shortwave and longwave band opacities in Exo-FMS to match our 1D HELIOS correlated-k results. Therefore, the double-gray opacities in our Exo-FMS roughly represent the opacities from the self-consistent  $100\times$  solar metallicity composition. The input parameters are listed in Table A1 and the temperature and wind structures can be found in Figure C1.

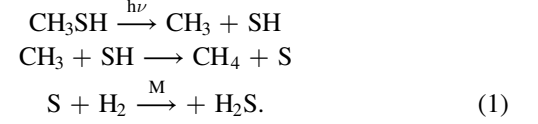
The temperatures and winds obtained from Exo-FMS are averaged over the equatorial region across  $30^\circ$  and divided into 32 longitude columns to set up VULCAN 2D. In VULCAN 2D, the zonal winds from the GCM are directly implemented for east–west advection, while vertical transport is parameterized by the eddy diffusion coefficient ( $K_{zz}$ ) derived from the mixing length theory with  $K_{zz} = 0.1 H \times w_{\text{rms}}$ , assuming  $0.1 \times H$  (scale height) as the characteristic length (Smith 1998; Charnay et al. 2015). We use the same lower-boundary conditions as the 1D model uniformly across all longitudes.

## 3. Results

### 3.1. 1D: $S_{\text{org}}$ Flux $\gtrsim 20\times$ Modern Earth Value Is Required to Accumulate ppm Levels of DMS

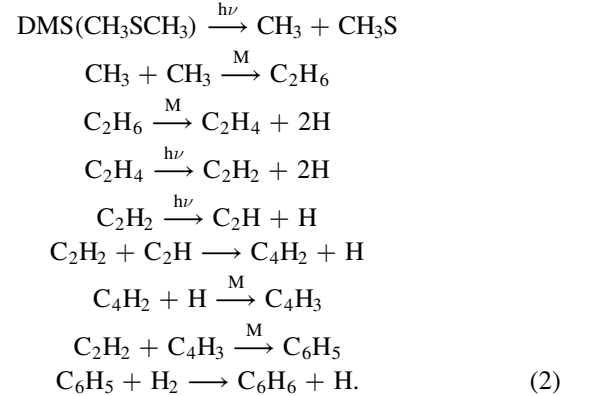
Figure 1 illustrates the average mixing ratios of several carbon-bearing and organic sulfur species in response to increases of biological production of sulfur gases. With modern Earth’s  $S_{\text{org}}$  flux, surface DMS reaches abundances of around 1–30 ppb, before being destroyed above 0.01 bar in our Hycean K2-18 b model. The DMS concentrations on Hycean K2-18 b are slightly higher than modern and Archean Earth’s values, which are around 0.01–1 ppb levels (Domagal-Goldman et al. 2011; Zhang et al. 2020). As the  $S_{\text{org}}$  flux continues increasing, there is an abrupt transition between 20 and 30 times  $S_{\text{org}}$  flux in our  $S_{\text{org}}$ -deposition-free setup. After this threshold, the atmosphere becomes rich in organic sulfur species and poor in CO, while  $\text{CH}_3\text{SH}$ , DMS, and DMDS jump from the sub-ppm level to above 0.1%. In the more conservative scenario where the ocean is not saturated, DMS is expected to be limited by the surface deposition and increased linearly with increasing  $S_{\text{org}}$ , as shown by the dashed line in Figure 1. Once  $S_{\text{org}}$  exceeds  $20\times$ – $30\times$  Earth’s value,  $\text{H}_2\text{S}$  begins accumulating in the upper atmosphere, as a result of photochemistry reducing sulfur back

to its thermochemically favored state. This occurs when  $\text{CH}_3\text{SH}$  builds up to sufficiently high abundances that its photodissociation becomes significant, producing  $\text{H}_2\text{S}$  via the following pathway:



In fact, the ultimate fate of  $S_{\text{org}}$  species in a Hycean atmosphere is either photochemical oxidation into  $\text{CH}_3\text{SO}$  or reduction back to hydrocarbons and  $\text{H}_2\text{S}$ , where  $\text{CH}_3\text{SO}$  is mainly produced by DMDS reacting with atomic O. The path to  $\text{H}_2\text{S}$  becomes more dominant over  $\text{CH}_3\text{SO}$  as  $S_{\text{org}}$  flux increases and makes the atmosphere more reducing. Although  $\text{SO}_2$  is also photochemically produced, it is highly soluble and deposition into the ocean limits abundances to insignificant levels.

Notably, the atmosphere also becomes rich in hydrocarbons as  $S_{\text{org}}$  increases, as pointed out in Domagal-Goldman et al. (2011). CO follows an opposite trend to  $S_{\text{org}}$ , showing an abrupt decline after 20 times modern Earth’s  $S_{\text{org}}$  flux. In this carbon-rich regime, the high abundances of haze precursors, such as  $\text{C}_4\text{H}_2$  and  $\text{C}_6\text{H}_6$  (Tsai et al. 2021), imply that the atmosphere would be covered by photochemical hazes (Arney et al. 2018). A main pathway to produce organic haze precursors in the upper atmosphere initiated by DMS photolysis is



For DMS at low concentrations below the ppm level, its primary sink is direct photodissociation. After the transition to where DMS has a high concentration, its photodissociation halts in the lower atmosphere due to shielding by DMDS,  $\text{CH}_3\text{SH}$ , and self-shielding. The reaction with atomic H becomes the main sink. This shielding effect from  $S_{\text{org}}$  also reduces the photolysis of  $\text{CO}_2$  causing the drop of CO when the flux  $\gtrsim 20\times S_{\text{org}}$ . The overall impact of shielding across this transition is evident in the top left panel of Figure 2, where DMS, DMDS, and  $\text{CH}_3\text{SH}$  significantly elevate the near-UV (NUV) photosphere and subsequently attenuate the NUV flux reaching the surface.

For an equivalent solar flux, the same average abundances of hydrocarbon and sulfur gases as a function of biological sulfur flux are shown in the bottom of Figure 1. One major difference is that the stronger NUV irradiation generates atomic H down to the surface, which significantly suppresses DMS and other organic sulfur gases. DMS remains below 10 ppb level for  $S_{\text{org}}$  flux up to 200 times modern Earth’s value. Moreover, the concentration of DMS is confined near the surface, whereas for

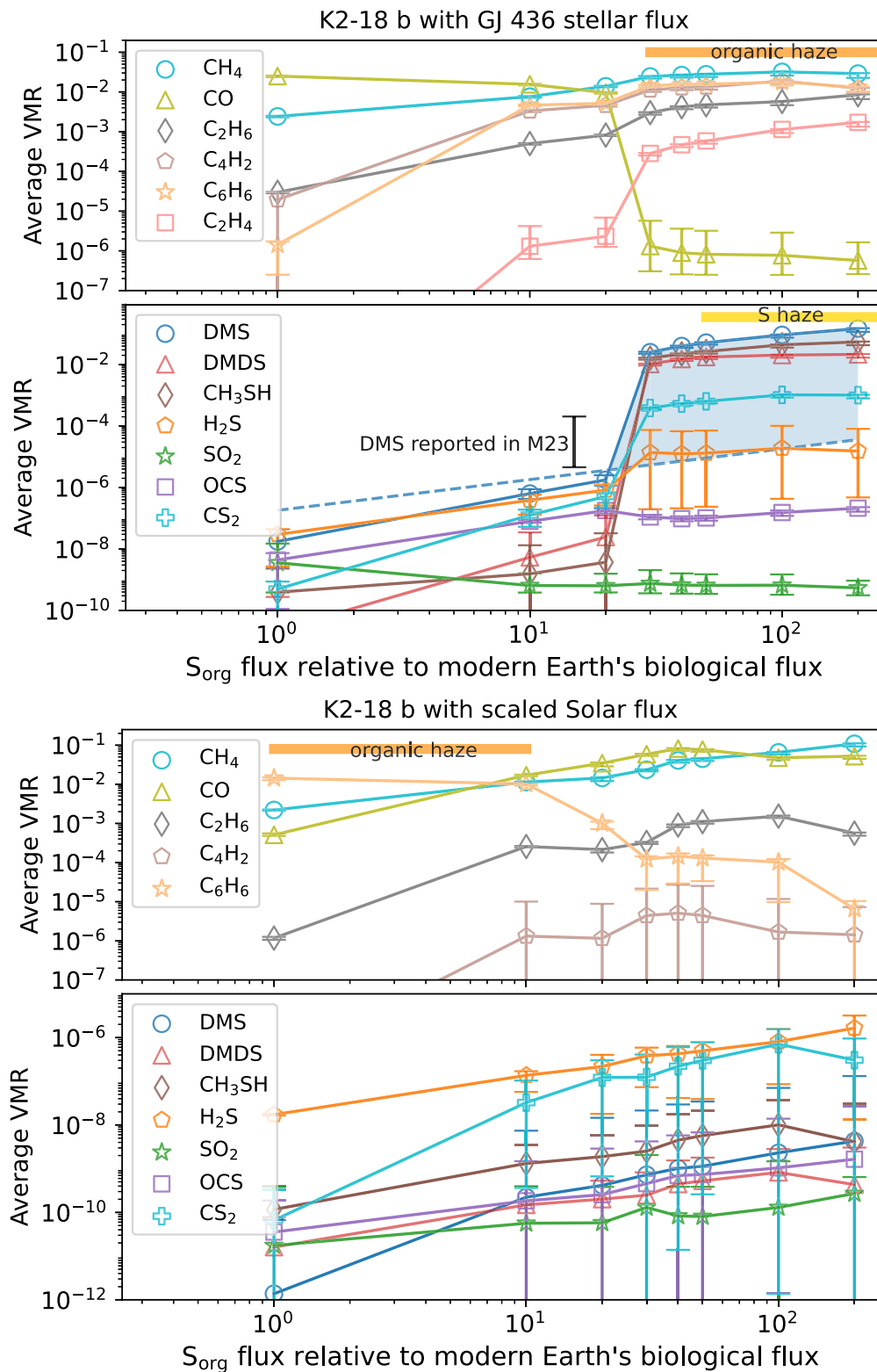


**Figure 1.** The average volume mixing ratios (VMRs) as a function of sulfur biological flux ( $S_{\text{org}}$ ). We adopt the stellar spectrum of GJ 436 as an analogous star to K2-18 for our nominal Hycean K2-18 b model (top). Additionally, we scaled the solar flux to match an equivalent flux (bottom). Open circles are the average VMRs across the  $1\text{--}10^{-4}$  bar pressure range, whereas error bars denote the full span of VMRs within this pressure range. The dashed line represents the limit of DMS given by surface deposition with  $0.01\text{ cm}^{-1}$  dry deposition velocity. Combined with the deposition-free DMS abundances in our model, the shaded blue region illustrates the upper and lower bounds of DMS abundance. The black error bar marks the reported DMS VMR from Madhusudhan et al. (2023; M23). The orange band highlights the regime where hydrocarbon haze precursors,  $\text{C}_4\text{H}_2$  and  $\text{C}_6\text{H}_6$ , exceed 1%. Similarly, the yellow band highlights the regime where elemental sulfur ( $\text{S}_8$ ) becomes saturated and condenses.

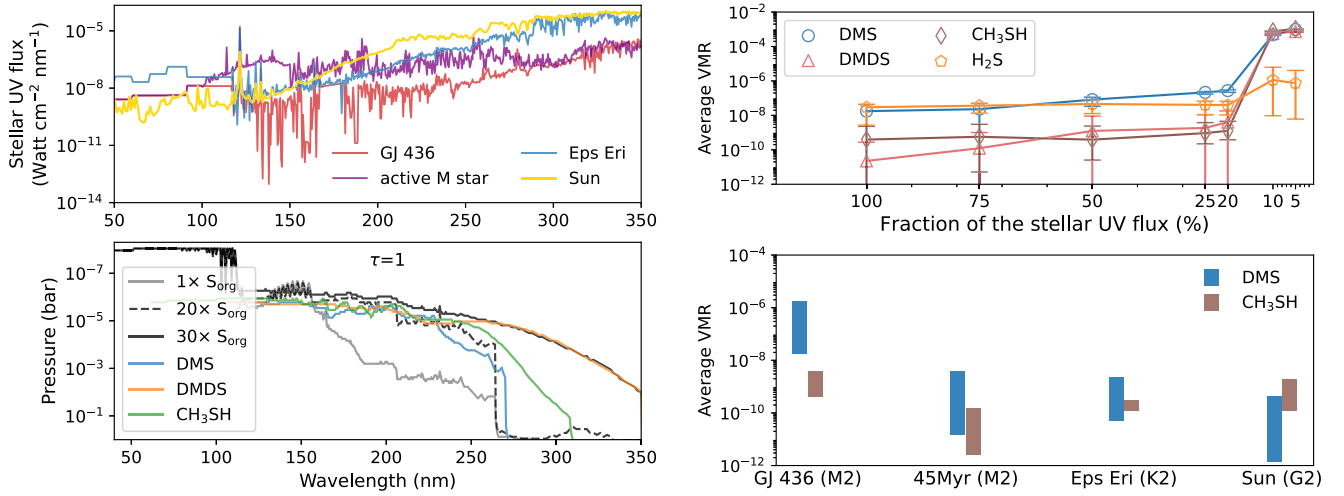


**Figure 2.** Left: the stellar spectra in the UV for GJ 436 (M2.5), a young (45 Myr) and active M star, Epsilon Eridani, and the Sun in the top panel. The spectra of GJ 436 and Epsilon Eridani are from the MUSCLES survey (version 2.2; France et al. 2016; Loyd et al. 2016; Youngblood et al. 2016), the active M star spectrum is from HAZMAT (Peacock et al. 2020), and the solar spectrum is from Gueymard (2018). The lower panel shows the UV photosphere ( $\tau = 1$ ) with different  $S_{\text{org}}$ . The contributions from DMS, DMDS, and  $\text{CH}_3\text{SH}$  are further displayed for the  $30\times S_{\text{org}}$  model. Right: the upper panel shows the average VMRs of several sulfur species as a function of attenuating total stellar UV flux for Earth’s  $S_{\text{org}}$  flux. The bottom panel shows the span of abundance averaged between 1 and  $10^{-4}$  bar for  $1\times$ – $20\times S_{\text{org}}$  flux around different stellar types.

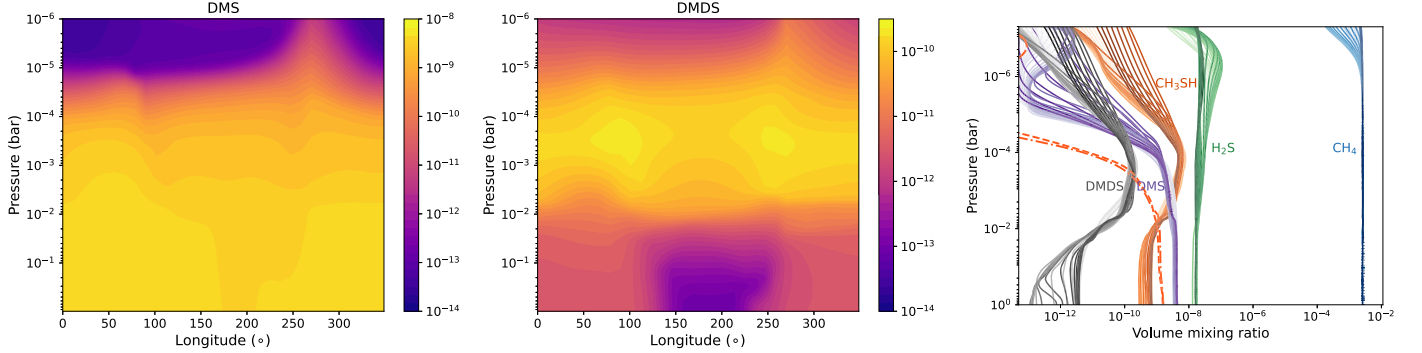


**Figure 3.** The equatorial volume-mixing-ratio distribution of DMS (left) and DMDS (middle) in our Hycean K2-18 b model with modern Earth  $S_{\text{org}}$  flux, computed by VULCAN 2D. The substellar point is located at  $180^\circ$  longitude. The right panel depicts the vertical distribution of several species across the equatorial region, where different shades correspond to different longitudinal locations. The vertical profiles of DMS excluding zonal transport are shown in red dotted (morning terminator,  $73^\circ$  westward substellar point) and dashed–dotted (evening terminator,  $73^\circ$  eastward substellar point) lines for comparison.

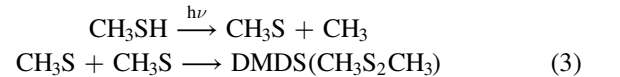
an M dwarf host star, DMS can extend vertically above 0.01 bar. Since  $S_{\text{org}}$  never reaches significant abundances under a Sun-like star, shielding of  $\text{CO}_2$  photolysis does not occur. Consequently, both  $\text{CH}_4$  and  $\text{CO}$  progressively increase with  $S_{\text{org}}$  flux. Our model results with an active M star show qualitatively similar trends to those with the equivalent solar flux owing to its enhanced UV flux.

### 3.2. 2D: DMS Is Homogenized by Global Circulation

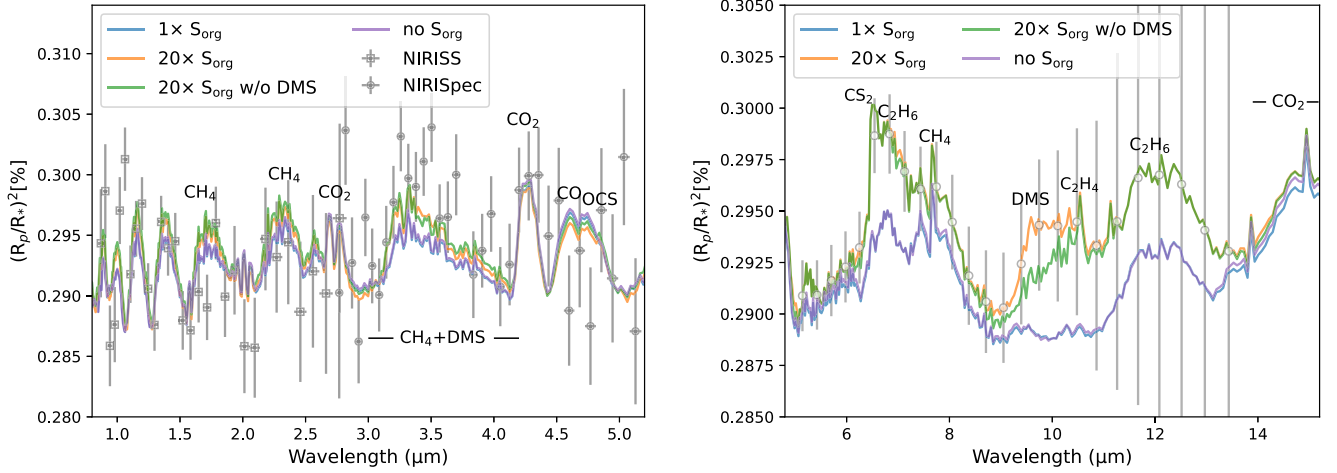
The temperature and wind structures simulated by our Hycean K2-18 b GCM can be found in Figure C1. The circulation exhibits an eastward zonal jet in the troposphere and day–night thermally driven cells in the stratosphere. In the upper atmosphere above  $10^{-4}$  bar, the flow transitions to retrograde, likely due to vertical momentum transport (Tsai et al. 2014). The mean tropospheric zonal wind below 0.01 bar is about  $20 \text{ m s}^{-1}$ , consistent with the jet speed estimated from wave balance (Hammond et al. 2020). This zonal wind speed translates to a horizontal transport timescale of  $\sim 10$  days.

Figure 3 illustrates the equatorial distribution of DMS and DMDS for modern Earth  $S_{\text{org}}$  production. DMS exhibits a rather uniform abundance below  $10^{-4}$  bar. As the zonal winds

change to retrograde in the upper atmosphere, DMS extends to higher altitudes around the evening terminator due to the westward transport from the nightside. On the other hand, DMDS is photochemically produced by  $\text{CH}_3\text{SH}$  via



in the stratosphere between  $10^{-2}$ – $10^{-4}$  bar and follows the thermally driven cells. This relatively uniform distribution of DMS can be understood by comparing relevant timescales. The photochemical lifetime of DMS on the dayside ( $\tau_{\text{DMS}}^{\text{day}}$ ) is determined by  $\tau_{\text{DMS}}^{\text{day}} = 1/k_{\text{DMS}}$ , where  $k_{\text{DMS}}$  is its photolysis rate.  $\tau_{\text{DMS}}^{\text{day}}$  is  $\sim 10^8$ – $10^9$  s in the troposphere below  $10^{-2}$  bar. On the nightside, the replenish timescale ( $\tau_{\text{DMS}}^{\text{night}}$ ) is given by  $\sim H/K_{\text{zz}}^2 \sim 10^8$  s. Given that  $\tau_{\text{DMS}}^{\text{day}}$  and  $\tau_{\text{DMS}}^{\text{night}}$  are comparable to each other and considerably longer than the horizontal transport timescale of  $\sim 10^6$  s, the  $S_{\text{org}}$  species on the nightside is still constrained by the photochemical processes on the dayside through global transport. We note that our 2D model already assumes an optimistic scenario with a uniform  $S_{\text{org}}$  flux across



**Figure 4.** Synthetic transmission spectra of Hycean K2-18 b 1D models for  $1\times$  and  $20\times$  modern Earth biological sulfur flux. The JWST NIRISS/SOSS and NIRSpec/G395H data from (Madhusudhan et al. 2023) are plotted in the left panel. The simulated noise by Pandexo (Batalha et al. 2017) with the JWST/MIRI LRS for five transits without random noise is plotted in the right panel (gray error bars). The  $20\times S_{\text{org}}$  spectrum but with DMS opacity removed is shown for comparison. The “no  $S_{\text{org}}$ ” case includes a flux for  $\text{CH}_4$  equivalent to modern Earth’s nonanthropogenic emission (Domagal-Goldman et al. 2011), but omits fluxes for all biogenic sulfur gases. The corresponding abundance profiles used to produce the spectra can be found in Figure C2.

the nightside. In reality, the nightside  $S_{\text{org}}$  flux might be much lower due to the lack of stellar energy input to power a (hypothetical) photosynthetic biosphere. Overall, the DMS abundance predicted by our 2D photochemical model is broadly consistent with that from 1D model, as indicated by the right panel in Figure 3.

### 3.3. Transmission Spectra

We simulated synthetic transmission spectra of our cloud-/haze-free Hycean K2-18 b models using PLATON (Zhang et al. 2019, 2020), including opacity sources of  $\text{CH}_4$ ,  $\text{CO}$ ,  $\text{CO}_2$ ,  $\text{C}_2\text{H}_2$ ,  $\text{H}_2\text{O}$ ,  $\text{HCN}$ ,  $\text{NH}_3$ ,  $\text{O}_2$ ,  $\text{NO}$ ,  $\text{C}_2\text{H}_4$ ,  $\text{C}_2\text{H}_6$ ,  $\text{H}_2\text{CO}$ ,  $\text{N}_2$ ,  $\text{NO}_2$ ,  $\text{H}_2\text{S}$ ,  $\text{COS}$ ,  $\text{SH}$ ,  $\text{SO}_2$ , (CIA) of  $\text{H}_2$ - $\text{H}_2$ , and  $\text{H}_2$ -He. We further include cross sections of  $\text{CH}_3\text{SH}$ , DMS, and DMS from the Pacific Northwest National Laboratories (PNNL) database (Johnson et al. 2004), which are limited to 1 bar pressure and room temperature.

The transmission spectra for none,  $1\times$  and  $20\times$  modern Earth  $S_{\text{org}}$  flux are compared in Figure 4. For the JWST NIRISS and NIRSpec coverage below  $5\ \mu\text{m}$ , all of our Hycean K2-18 b models with methanogenic flux produce  $\text{CH}_4$  absorption features between 1 and  $4\ \mu\text{m}$  that are broadly consistent with the JWST data. However, it is challenging to distinguish the DMS absorption contribution within the NIRSpec coverage, even with  $20\times S_{\text{org}}$  flux. The signal of DMS around  $3.5\ \mu\text{m}$  for  $20\times S_{\text{org}}$  flux does not exceed 10 ppm, smaller than NIRSpec’s precision of 30–50 ppm at  $R \sim 50$  (Madhusudhan et al. 2023). The most promising diagnostics window of DMS is in the mid-infrared, as indicated in the right panel of Figure 4. For the  $20\times S_{\text{org}}$  case, DMS and the photochemical byproduct  $\text{C}_2\text{H}_4$  contribute to an absorption of about 50 ppm at 9–11  $\mu\text{m}$ , in addition to the  $\text{C}_2\text{H}_6$  feature at 7  $\mu\text{m}$ . The 7  $\mu\text{m}$  feature of  $\text{C}_2\text{H}_6$  also overlaps with  $\text{CS}_2$ , making it difficult to differentiate the contribution of  $\text{CS}_2$ . Our transmission spectra reveal no discernible  $\text{H}_2\text{S}$  spectral signatures. While  $\text{H}_2\text{S}$  can reach above ppm levels with outgassing and photochemical sources (e.g., Equation (1)), its broad opacities that overlap with several species make it challenging to detect.

Since ethane ( $\text{C}_2\text{H}_6$ ) is efficiently produced from  $\text{CH}_4$  and has strong mid-infrared absorption bands,  $\text{C}_2\text{H}_6$  shows a prominent feature at 7 and 11–13  $\mu\text{m}$  with or without the presence of  $S_{\text{org}}$

**Table 1**  
Detectability of Potential Biosignature Gases with Corresponding Wavelength Ranges on Hycean K2-18 b Based on Our Models with  $1\times$ – $20\times S_{\text{org}}$  Flux

Species	1–5 $\mu\text{m}$	5–15 $\mu\text{m}$
$\text{CH}_4$	✓	✓
$\text{CO}_2$	✓	✓
$\text{H}_2\text{S}$	✗	✗
$\text{CH}_3\text{SH}$	✗	✗
$\text{CS}_2$	✗	?
DMS	✗	?
DMDS	✗	✗
$\text{C}_2\text{H}_4$	✗	?
$\text{C}_2\text{H}_6$	✗	✓

**Note.** ✓ denotes detectable ( $\gtrsim 50$  ppm) and ✗ denotes nondetectable ( $\lesssim 10$  ppm), whereas ? means challenging, with shallow features ( $\gtrsim 20$  ppm but  $\lesssim 50$  ppm) and only present under enhanced  $20\times S_{\text{org}}$  flux.

flux. By constraining  $[\text{CH}_4]/[\text{C}_2\text{H}_6]$ , one can potentially estimate the relative contribution of methanogenic  $\text{CH}_4$  flux relative to  $S_{\text{org}}$  flux (Domagal-Goldman et al. 2011). Since our model likely overpredicts  $\text{C}_6\text{H}_6$  in the gas phase due to the lack of conversion to higher-order hydrocarbons and particles, we did not include  $\text{C}_6\text{H}_6$  opacities when generating the spectra in Figure 4. However, it is interesting to keep in mind that the presence ( $\gtrsim 50$  ppm) of  $\text{C}_6\text{H}_6$  would exhibit detectable features within NIRSpec wavelength range, in addition to  $\text{CH}_4$  and  $\text{CO}_2$  (see Figure C3). For biogenic flux  $\gtrsim 30\times$  Earth’s  $S_{\text{org}}$  flux, the atmospheric mean molecular weight exceeds 8 amu in addition to the expected aerosols that would flatten transmission spectral features, making it immediately distinguishable for  $\lesssim 20\times$  cases. We summarize the identifiable biosignature features with  $1\times$ – $20\times S_{\text{org}}$  flux in Table 1.

## 4. Discussion

Since K2-18 b requires reflective clouds and hazes to sustain water oceans, we explore the potential UV shielding effects due to clouds and hazes in the bottom panel of Figure 2. Organic sulfur species only start to build up when the stellar UV is reduced to less than 20%. For K2-18 b specifically,

Leconte et al. (2024) highlighted the observed methane features deeper than  $\sim 100$  ppm (their Figure 9) are not consistent with highly reflective clouds. We argue that our photochemical results should remain robust to UV attenuation by clouds and hazes, unless muted spectral features indicate scattering by high-altitude aerosols can significantly reduce stellar UV flux.

The predicted requirement of  $20\times S_{\text{org}}$  flux to be potentially detectable is equivalent to about  $0.004 \text{ g m}^{-2}$  based on the DMS lab production rate (Seager et al. 2013), which is within the plausible range of surface biomass density. Our predictions for the biogenic sulfur gases in Hycean atmospheres are broadly consistent with previous studies of the Archean Earth Domagal-Goldman et al. (2011) and Archean-like atmospheres on Trappist-1 planets (Meadows et al. 2023). While Meadows et al. (2023) concluded  $\text{CH}_3\text{SH}$  to be the most prominent  $S_{\text{org}}$  feature in  $\text{N}_2$ -dominated atmospheres, we find efficient  $\text{CH}_3\text{SH}$  conversion into  $\text{H}_2\text{S}$  in a  $\text{H}_2$  atmosphere. Consequently, DMS appears to constitute the most detectable organic sulfur molecule in the mid-infrared for Hycean worlds.

On modern Earth, the oxidation of DMS might participate in the sulfuric cloud formation (Charlson et al. 1987) and affect climate feedback. It has been suggested that this biologically driven feedbacks could help stabilize the Earth's climate (Lovelock 1989), although the precise pathways and quantified contributions from DMS to aerosols still remain elusive. Similarly, on a Hycean world with highly elevated  $S_{\text{org}}$  flux ( $\gtrsim 30\times$  modern Earth's value; see Figure 1), hydrocarbon and elemental sulfur hazes ( $S_8$ ) are expected to form. We speculate a similar negative feedback loop can take place in a Hycean world, where photochemical hazes derived from organic sulfur flux can increase albedo and prevent a runaway state.

Lastly, we reiterate that constructing complete line lists for DMS, DMDS, and  $\text{CH}_3\text{SH}$  to correctly account for the pressure-broadening effects would improve the interpretation of spectral data. Future work extending the study encompassing the diversity of halomethanes, such as methyl chloride and methyl bromide (e.g., Leung et al. 2022), will expand our understanding of the biosignature gases on sub-Neptune waterworlds.

## 5. Conclusion

We find a biogenic sulfur flux of approximately 20 times higher than modern Earth's is required for DMS to reach detectable levels (i.e., above  $\sim$ ppm) on a K2-18 b-like Hycean world. At the terminators, our 2D photochemical model shows only minor abundance enhancements in DMS compared to 1D model predictions. On the other hand, JWST/MIRI could detect  $\text{C}_2\text{H}_6$  around  $7 \mu\text{m}$  and the broad feature at  $9\text{--}13 \mu\text{m}$  contributed from DMS,  $\text{C}_2\text{H}_4$ , and  $\text{C}_2\text{H}_6$  with  $20\times S_{\text{org}}$  flux, based on our fiducial Hycean model. However, identifying DMS signatures within NIRSpec's wavelength range is demonstrated to be challenging, despite DMS appearing as the most promising biogenic sulfur signature directly from the  $S_{\text{org}}$  source. The moderate threshold for biological production suggests that the search for biogenic sulfur gases as one class of potential biosignature is plausible for Hycean worlds.

## Acknowledgments

The authors thank Michaela Leung for the useful comments on an early draft of this article. The authors also thank Stephen Klippenstein and Julie I. Moses for the illuminating discussion on  $\text{H}_2\text{CO}$  kinetics and for sharing the ab initio calculations. S.-M.T.

thanks Eva-Maria Ahrer, Guangwei Fu, Jake Taylor, and Lili Alderson for helpful discussions on data resampling and feature identification. S.-M.T. and E.W.S. acknowledge support from National Aeronautics and Space Administration (NASA) through Exobiology grant No. 80NSSC20K1437 and Interdisciplinary Consortia for Astrobiology Research (ICAR) grant Nos. 80NSSC23K1399, 80NSSC21K0905, and 80NSSC23K1398. H.I. is funded by the European Union (ERC, DIVERSE, 101087755, and ERC, EXOCONDENSE, 740963). Views and opinions expressed are however those of the author(s) only and do not necessarily reflect those of the European Union or the European Research Council Executive Agency. Neither the European Union nor the granting authority can be held responsible for them. N.F.W. was supported by the NASA Postdoctoral Program.

*Software:* Exo-FMS (Lee et al. 2020, 2021), VULCAN (Tsai et al. 2017, 2021), Numpy (van der Walt et al. 2011).

## Appendix A Model Input Parameters

Table A1 lists the input parameters for Hycean K2-18 b with the HELIOS radiative transfer model and the Exo-FMS general circulation model. HELIOS includes  $\text{H}_2\text{O}$ ,  $\text{CH}_4$ ,  $\text{CO}$ ,  $\text{CO}_2$ ,  $\text{NH}_3$ ,  $\text{HCN}$ ,  $\text{C}_2\text{H}_2$ , collision-induced absorption (CIA) of  $\text{H}_2\text{--H}_2$  and  $\text{H}_2\text{--He}$  as opacity sources. We ignore the  $\text{H}_2\text{O}$  self continuum absorption and likely underestimate the tropospheric temperature. Exo-FMS uses double-gray opacities for its radiative transfer. The optical depth in the infrared ( $\tau_{\text{IR}}$ ) and shortwave ( $\tau_{\text{SW}}$ ) bands is given by

$$d\tau_i = (\kappa_{i,d}(1 - q) + \kappa_{i,w}q)(f_i + 2(1 - f_i)) \left( \frac{p}{p_s} \right) \frac{dp}{p_s}, \quad (\text{A1})$$

where the  $i$  subscript represents either the SW or IR band,  $p$  is the pressure, and  $p_s$  the surface pressure. The opacities  $\kappa_{i,w}$  and

**Table A1**  
Planetary Parameters for Hycean K2-18 b

Symbol	Value	Unit	Description
$R_p$	$1.66 \times 10^7$	m	Planetary radius
$a$	0.1591	au	Orbital distance
$T_{\text{irr}}$	1370	K	Irradiation temperature
$T_{\text{int}}$	0	K	Internal temperature
$g$	12.43	$\text{m s}^{-2}$	Gravitational acceleration
$c_p$	2216	$\text{J K}^{-1} \text{kg}^{-1}$	Specific heat capacity
$\Omega_p$	$2.2137 \times 10^{-6}$	$\text{rad s}^{-1}$	Planetary rotation rate

**Table A2**  
Radiative Parameters for the Exo-FMS Double-gray Radiation Scheme

Symbol	Value	Unit	Description
$\kappa_{\text{IR},d}$	$1.15 \times 10^{-3}$	$\text{m}^2 \text{kg}^{-1}$	IR dry opacity
$\kappa_{\text{IR},w}$	$1 \times 10^{-2}$	$\text{m}^2 \text{kg}^{-1}$	IR water opacity
$\kappa_{\text{SW},d}$	$2 \times 10^{-5}$	$\text{m}^2 \text{kg}^{-1}$	SW dry opacity
$\kappa_{\text{SW},w}$	$4 \times 10^{-4}$	$\text{m}^2 \text{kg}^{-1}$	SW water opacity
$\kappa_{\text{SW},2}$	$5 \times 10^{-2}$	$\text{m}^2 \text{kg}^{-1}$	SW second band opacity
$\alpha$	$1 \times 10^{-2}$	Dimensionless	Fraction of instellation in SW second band
$f_{\text{IR}}$	0.9	Dimensionless	Controls pressure dependence of $\tau_{\text{IR}}$
$f_{\text{SW}}$	0.2	Dimensionless	Controls pressure dependence of $\tau_{\text{SW}}$

$\kappa_{i,d}$  represent the opacities due to the water vapor component and dry component (all other gases) of the atmosphere respectively. The factor  $f_i$  accounts for pressure dependence of opacity, due to collision-induced absorption and pressure-broadening effects. To reproduce the inversion in the HELIOS calculations, a second band was added in the SW part of the spectrum, receiving a fraction  $\alpha$  of the total incoming flux. The optical depth in this band was given by

$$\tau_{SW,2} = \frac{\kappa_{SW,2}P}{g}. \quad (\text{A2})$$

The water mass concentration,  $q$ , used in this calculation is taken from the 1D HELIOS calculation and remains constant throughout the simulation (though in reality this should be spatially inhomogeneous and linked to the local saturation vapor pressure at a given temperature and pressure). The value of  $\kappa_{IR,w}$  was taken to match the runaway greenhouse OLR of  $\approx 280 \text{ Wm}^{-2}$  (as in Innes et al. 2023). The other values were tuned to match the HELIOS temperature-pressure profile. The parameters used are shown in Table A2.

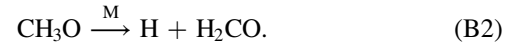
### Appendix B Updated H<sub>2</sub>CO Reaction Rates

Formaldehyde (H<sub>2</sub>CO) is one of the main intermediate species in CO<sub>2</sub>-CO-CH<sub>4</sub> interconversion. Forming and breaking the double bond between C and O in H<sub>2</sub>CO may facilitate

an important step that controls the overall timescale (Tsai et al. 2018). There are two three-body reactions involving H<sub>2</sub>CO that we adopt the thermal dissociation rate coefficients due to the lack of low-pressure rate limits for recombination:



and



The recombination rates are then reversed by thermochemical data. In the default chemical networks in VULCAN (e.g., NCHO\_photo\_network<sup>8</sup>), the adopted rate coefficients either underestimate the activation energy or are only valid at high temperatures. As a result, these reversed rates tend to overpredict the CO<sub>2</sub>-CH<sub>4</sub> conversion efficiency around room temperatures. In this study, we have adopted the low-pressure rate coefficients for Equations (B1) and (B2) from Tsang & Hampson (1986) and Tsang (1987), which are more consistent with the ab initio calculations conducted by S. J. Klippenstein (2023, private communication). The original and updated rate coefficients are summarized in Table B1. This update of H<sub>2</sub>CO kinetics significantly lowers the CH<sub>4</sub> abundance in our lifeless case (without methanogenic flux; Figure B1) from  $\sim 10^{-5}$  to  $\sim 10^{-8}$ , which is consistent with the calculations in Wogan et al. (2024).

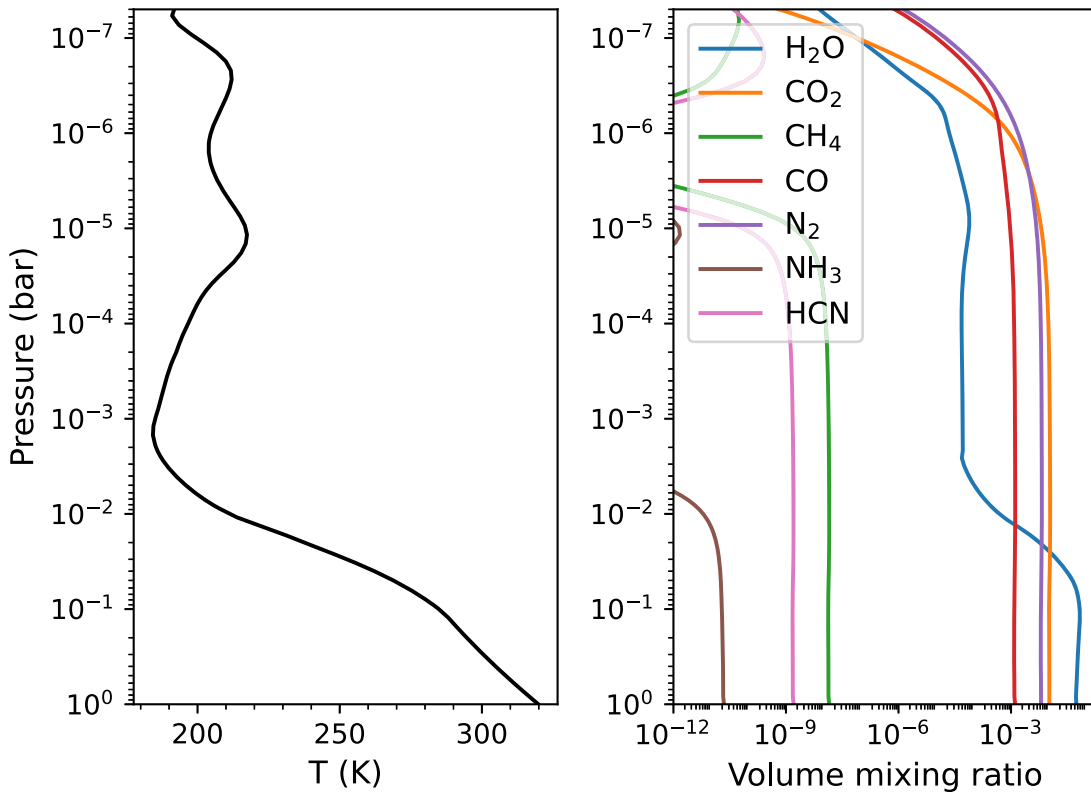


**Figure B1.** The self-consistent temperature (left) and composition (right) profiles generated by iterative runs between HELIOS and VULCAN. Sulfur kinetics is not included in the VULCAN runs here for simplicity.

<sup>8</sup> [https://github.com/exoclimate/VULCAN/blob/master/thermo/NCHO\\_photo\\_network.txt](https://github.com/exoclimate/VULCAN/blob/master/thermo/NCHO_photo_network.txt)



**Table B1**  
Updated H<sub>2</sub>CO Reaction Rate Coefficients

Reactions	Rate Coefficients <sup>a</sup>	Reference
Original		
$\text{CH}_2\text{OH} \xrightarrow{\text{M}} \text{H} + \text{H}_2\text{CO}$	$k_0 = 1.66 \times 10^{-10} \exp(-12630/T)$ $k_\infty = 3 \times 10^9 \exp(-14640/T)$	Tsuboi et al. (1981), Cribb et al. (1992)
$\text{CH}_3\text{O} \xrightarrow{\text{M}} \text{H} + \text{H}_2\text{CO}$	$k_0 = 9 \times 10^{-11} \exp(-6790/T)$ $k_\infty = 1.56 \times 10^{15} T^{-0.39} \exp(-13300/T)$	Baulch et al. (1994), Curran (2006)
Updated		
$\text{CH}_2\text{OH} \xrightarrow{\text{M}} \text{H} + \text{H}_2\text{CO}$	$k_0 = 7.48 \times 10^1 T^{-2.5} \exp(-17200/T)$ $k_\infty = 4.53 \times 10^{34} T^{-7.11} \exp(-22200/T)$	Tsang (1987) Xu et al. (2015)
$\text{CH}_3\text{O} \xrightarrow{\text{M}} \text{H} + \text{H}_2\text{CO}$	$k_0 = 6.51 \times 10^{13} T^{-6.65} \exp(-16700/T)$ $k_\infty = 3.17 \times 10^{24} T^{-4.25} \exp(-13100/T)$	Tsang & Hampson (1986) Xu et al. (2015)

**Note.**

<sup>a</sup> In low pressure rate coefficient,  $k_0$  ( $\text{cm}^6 \text{ molecules}^{-2} \text{ s}^{-1}$ ), and high pressure rate coefficient,  $k_\infty$  ( $\text{cm}^3 \text{ molecules}^{-1} \text{ s}^{-1}$ ).

### Appendix C Model Supplements

The lower boundary conditions for our inhabited Hycean model are listed in Table C1. Figure C1 presents the output of the Exo-FMS model, while Figure C2 summarizes the abundance profiles from the Hycean K2-18b 1D photochemical models. Additionally, Figure C3 demonstrates the spectral feature of C<sub>6</sub>H<sub>6</sub>.

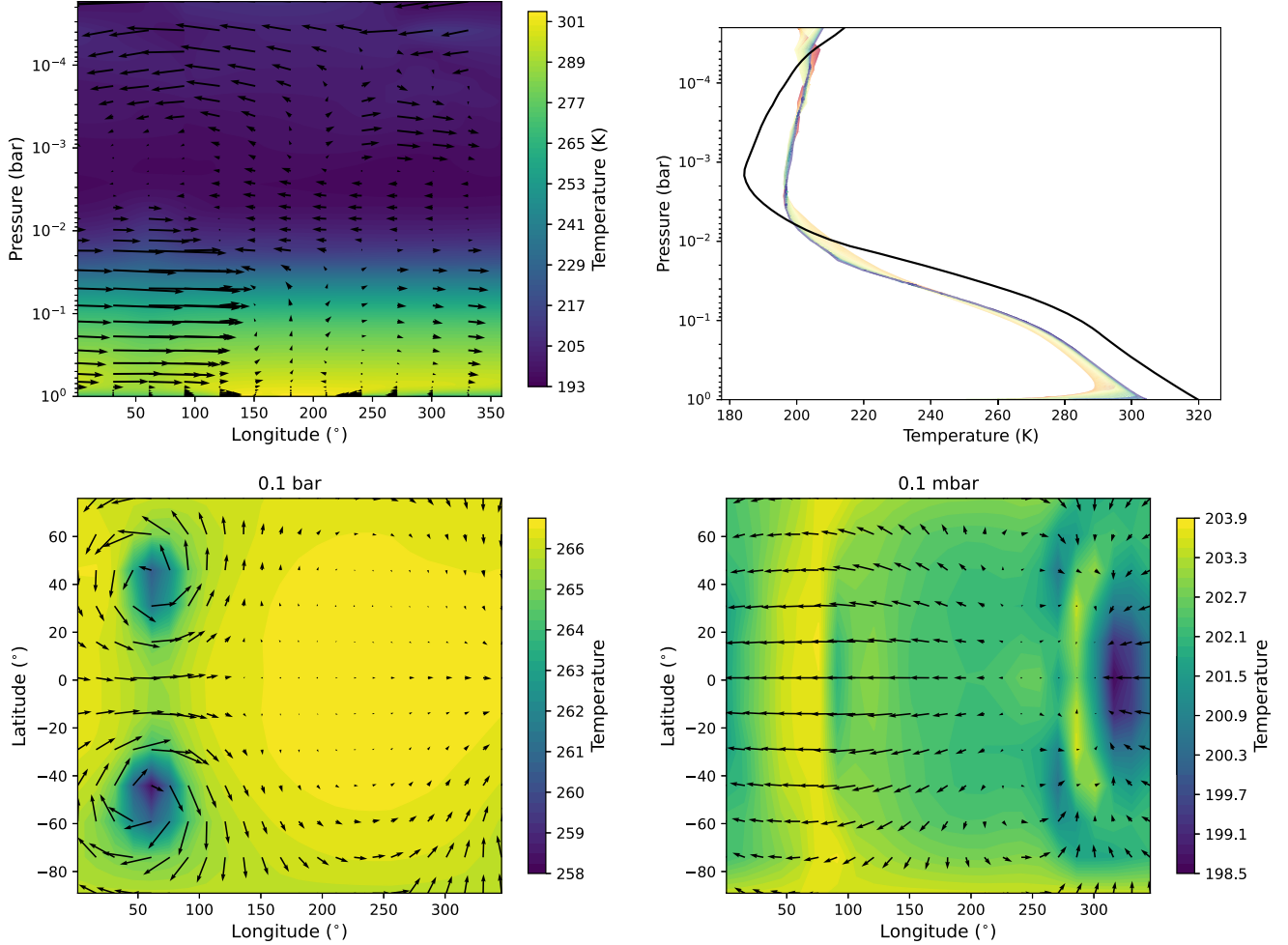


**Figure C1.** The top left panel shows the temperatures (color scale) and winds (arrows) on the equatorial plane averaged across  $\pm 30^\circ$  latitudes from our K2-18 b GCM (substellar point located at  $180^\circ$  longitude). The top right panel displays the vertical temperature profiles around the equator corresponding to different longitudinal locations, where the temperature profile from the 1D radiative transfer calculation (HELIOS) is plotted in black for comparison. The bottom two panels show the temperatures and winds at 0.1 bar and 0.1 mbar level.

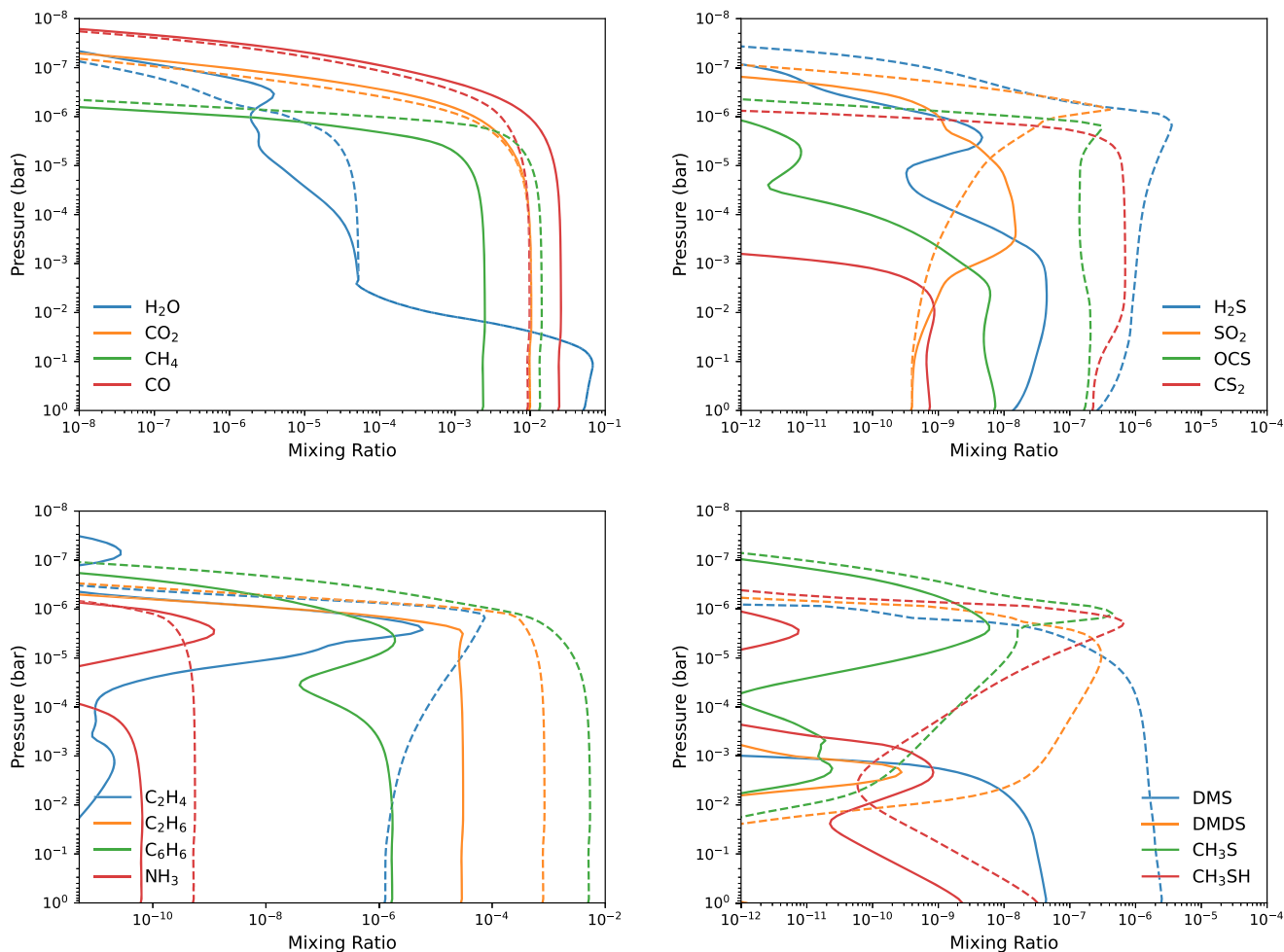


**Figure C2.** The abundance profiles of the Hycean K2-18 b 1D models with  $1\times$  (solid) and  $20\times$  (dashed) modern Earth values.

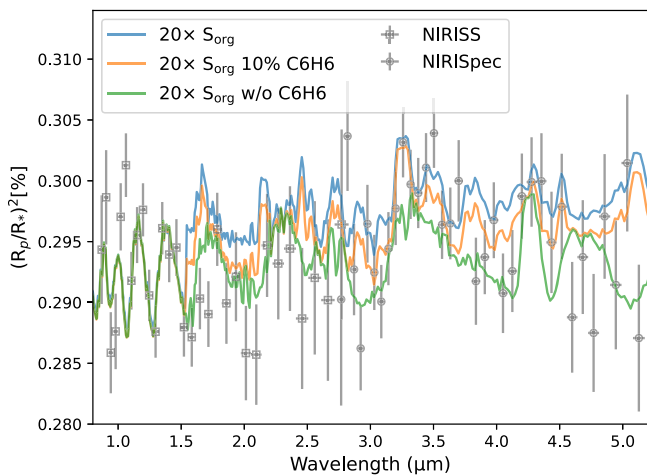


**Figure C3.** Synthetic transmission spectra of Hycean K2-18 b similar to Figure 4, but including  $C_6H_6$  absorption for  $20\times S_{org}$  flux. The spectra without  $C_6H_6$  opacity and with 10% of  $C_6H_6$ , representing depletion from haze formation, are shown for comparison.

**Table C1**

Lower-boundary Conditions for Photochemical Modeling of Inhabited Hycean K2-18 b

Species	Surface Emission (molecules $cm^{-2}$ $s^{-1}$ )	Vdep ( $cm$ $s^{-1}$ )
$CH_4^a$	$7 \times 10^{10}$	0
$CH_3SH^a$	$8.3 \times 10^8$	0
$DMS^a$	$4.2 \times 10^9$	$0^d$
$CS_2^a$	$1.4 \times 10^7$	0
$H_2S^b$	$2 \times 10^8$	0.015
$SO_2^b$	$9 \times 10^9$	1
$COS^b$	$5.4 \times 10^7$	0.003
$H_2O_2^c$	0	1
$CH_3S^a$	0	0.01
$HSO^a$	0	1
$S^a$	0	1
$SO^a$	0	0.0003

**Notes.**



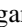

<sup>a</sup> Domagal-Goldman et al. (2011).

<sup>b</sup> Seinfeld & Pandis (2016).

<sup>c</sup> Hauglustaine et al. (1994).

<sup>d</sup> For the scenario that the surface layer of the ocean is saturated. The measured deposition velocity of DMS on land is  $0.064\text{--}0.28\text{ cm s}^{-1}$  (Judeikis & Wren 1977).

## ORCID iDs

Shang-Min Tsai  <https://orcid.org/0000-0002-8163-4608>  
 Hamish Innes  <https://orcid.org/0000-0001-5271-0635>  
 Nicholas F. Wogan  <https://orcid.org/0000-0002-0413-3308>  
 Edward W. Schwieterman  <https://orcid.org/0000-0002-2949-2163>

## References

- Arney, G., Domagal-Goldman, S. D., & Meadows, V. S. 2018, *AsBio*, **18**, 311  
 Batalha, N. E., Mandell, A., Pontoppidan, K., et al. 2017, *PASP*, **129**, 064501  
 Baulch, D. L., Cobos, C. J., Cox, R. A., et al. 1994, *JPCRD*, **23**, 847  
 Bean, J. L., Raymond, S. N., & Owen, J. E. 2021, *JGRE*, **126**, e06639  
 Benneke, B., Wong, I., Piaulet, C., et al. 2019, *ApJL*, **887**, L14  
 Cala, B. A., Archer-Nicholls, S., Weber, J., et al. 2023, *ACP*, **23**, 14735  
 Catling, D. C., & Zahnle, K. J. 2020, *SciA*, **6**, eaax1420  
 Charlson, R. J., Lovelock, J. E., Andreae, M. O., & Warren, S. G. 1987, *Natur*, **326**, 655  
 Charnay, B., Meadows, V., & Leconte, J. 2015, *ApJ*, **813**, 15  
 Chen, H., Wolf, E. T., Kopparapu, R., Domagal-Goldman, S., & Horton, D. E. 2018, *ApJL*, **868**, L6  
 Cribb, P. H., Dove, J. E., & Yamazaki, S. 1992, *CoFl*, **88**, 169  
 Curran, H. J. 2006, *Int. J. Chem. Kinet.*, **38**, 250  
 Domagal-Goldman, S. D., Meadows, V. S., Claire, M. W., & Kasting, J. F. 2011, *AsBio*, **11**, 419  
 Esparza-Borges, E., López-Morales, M., Adams Redai, J. I., et al. 2023, *ApJL*, **955**, L19  
 France, K., Loyd, R. O. P., Youngblood, A., et al. 2016, *ApJ*, **820**, 89  
 Gueymard, C. A. 2018, *SoEn*, **169**, 434  
 Hammond, M., Tsai, S.-M., & Pierrehumbert, R. T. 2020, *ApJ*, **901**, 78  
 Hauglustaine, D. A., Granier, C., Brasseur, G. P., & MéGie, G. 1994, *JGR*, **99**, 1173  
 House, C. H., Runnegar, B., & Fitz-Gibbon, S. T. 2003, *Gbio*, **1**, 15  
 Howard, A. W., Marcy, G. W., Bryson, S. T., et al. 2012, *ApJS*, **201**, 15  
 Hu, R., Damiano, M., Scheucher, M., et al. 2021, *ApJL*, **921**, L8  
 Hu, R., Seager, S., & Bains, W. 2012, *ApJ*, **761**, 166  
 Innes, H., & Pierrehumbert, R. T. 2022, *ApJ*, **927**, 38  
 Innes, H., Tsai, S.-M., & Pierrehumbert, R. T. 2023, *ApJ*, **953**, 168  
 Johnson, T. J., Sams, R. L., & Sharpe, S. W. 2004, *Proc. SPIE*, **5269**, 159  
 Judeikis, H. S., & Wren, A. G. 1977, *AtmEn*, **11**, 1221  
 Kettle, A. J., Rhee, T. S., von Hobe, M., et al. 2001, *JGR*, **106**, 12,193  
 Kite, E. S., & Ford, E. B. 2018, *ApJ*, **864**, 75  
 Leconte, J., Spiga, A., Clément, N., et al. 2024, arXiv:2401.06608  
 Lee, E. K. H., Parmentier, V., Hammond, M., et al. 2021, *MNRAS*, **506**, 2695  
 Lee, G. K., Casewell, S. L., Chubb, K. L., et al. 2020, *MNRAS*, **496**, 4674  
 Leung, M., Schwieterman, E. W., Parenteau, M. N., & Faucher, T. J. 2022, *ApJ*, **938**, 6  
 Li, C.-Y., Cao, H.-Y., Wang, Q., et al. 2023, *ISMEJ*, **17**, 1184  
 Lovelock, J. E. 1989, *RvGeo*, **27**, 215  
 Loyd, R. O. P., France, K., Youngblood, A., et al. 2016, *ApJ*, **824**, 102  
 Luque, R., & Pallé, E. 2022, *Sci*, **377**, 1211  
 Madhusudhan, N., Nixon, M. C., Welbanks, L., Piette, A. A. A., & Booth, R. A. 2020, *ApJL*, **891**, L7  
 Madhusudhan, N., Piette, A. A. A., & Constantinou, S. 2021, *ApJ*, **918**, 1  
 Madhusudhan, N., Sarkar, S., Constantinou, S., et al. 2023, *ApJL*, **956**, L13  
 Malik, M., Kempton, E. M. R., Koll, D. D. B., et al. 2019b, *ApJ*, **886**, 142  
 Malik, M., Kitzmann, D., Mendonça, J. M., et al. 2019a, *AJ*, **157**, 170  
 Mateos, K., Chappell, G., Klos, A., et al. 2023, *SciA*, **9**, eade4847  
 Meadows, V., Lincowski, A., & Lustig-Yaeger, J. 2023, AAS Meeting Abstracts, **55**, 125.04  
 Nixon, M. C., & Madhusudhan, N. 2021, *MNRAS*, **505**, 3414  
 Peacock, S., Barman, T., Shkolnik, E. L., et al. 2020, *ApJ*, **895**, 5  
 Pierrehumbert, R. T. 2023, *ApJ*, **944**, 20  
 Piette, A. A. A., & Madhusudhan, N. 2020, *ApJ*, **904**, 154  
 Pilcher, C. B. 2003, *AsBio*, **3**, 471  
 Rogers, J. G., Schlichting, H. E., & Owen, J. E. 2023, *ApJL*, **947**, L19  
 Schwieterman, E. W., Kiang, N. Y., Parenteau, M. N., et al. 2018, *AsBio*, **18**, 663  
 Seager, S., Bains, W., & Hu, R. 2013, *ApJ*, **777**, 95  
 Seinfeld, J. H., & Pandis, S. N. 2016, *Atmospheric Chemistry and Physics: from Air Pollution to Climate Change* (Hoboken, NJ: Wiley)  
 Smith, M. D. 1998, *Icar*, **132**, 176  
 Thompson, S. E., Coughlin, J. L., Hoffman, K., et al. 2018, *ApJS*, **235**, 38  
 Tsai, S.-M., Dobbs-Dixon, I., & Gu, P.-G. 2014, *ApJ*, **793**, 141  
 Tsai, S.-M., Innes, H., Lichtenberg, T., et al. 2021b, *ApJL*, **922**, L27  
 Tsai, S.-M., Kitzmann, D., Lyons, J. R., et al. 2018, *ApJ*, **862**, 31  
 Tsai, S.-M., Lyons, J. R., Grosheintz, L., et al. 2017, *ApJS*, **228**, 20  
 Tsai, S.-M., Malik, M., Kitzmann, D., et al. 2021, *ApJ*, **923**, 264  
 Tsai, S.-M., Moses, J. I., Powell, D., & Lee, E. K. H. 2023c, *ApJL*, **959**, L30  
 Tsai, S.-M., Parmentier, V., Mendonça, J. M., et al. 2024, *ApJ*, **963**, 41  
 Tsang, W. 1987, *JPCRD*, **16**, 471  
 Tsang, W., & Hampson, R. F. 1986, *JPCRD*, **15**, 1087  
 Tsiaras, A., Waldmann, I. P., Tinetti, G., Tennyson, J., & Yurchenko, S. N. 2019, *NatAs*, **3**, 1086  
 Tsuboi, T., Katoh, M., Kikuchi, S., & Hashimoto, K. 1981, *JaJAP*, **20**, 985  
 van der Walt, S., Colbert, S. C., & Varoquaux, G. 2011, *CSE*, **13**, 22  
 Venturini, J., Guilera, O. M., Haldemann, J., Ronco, M. P., & Mordasini, C. 2020, *A&A*, **643**, L1  
 Wogan, N. F., Batalha, N. E., Zahnle, K. J., et al. 2024, *ApJL*, **963**, L7  
 Xu, Z. F., Raghunath, P., & Lin, M. C. 2015, *JPCA*, **119**, 7404  
 Youngblood, A., France, K., Loyd, R. O. P., et al. 2016, *ApJ*, **824**, 101  
 Yu, X., Moses, J. I., Fortney, J. J., & Zhang, X. 2021, *ApJ*, **914**, 38  
 Zeng, L., Jacobsen, S. B., Sasselov, D. D., et al. 2019, *PNAS*, **116**, 9723  
 Zhang, M., Chachan, Y., Kempton, E. M. R., & Knutson, H. A. 2019, *PASP*, **131**, 034501  
 Zhang, M., Chachan, Y., Kempton, E. M. R., Knutson, H. A., & Chang, W. H. 2020, *ApJ*, **899**, 27  
 Zhang, M., Park, K.-T., Yan, J., et al. 2020, *PrOce*, **186**, 102392